J. Fluid Mech. (1992), *vol.* 240, *pp.* 503–532
Printed in Great Britain

Impingement of an axisymmetric jet on unheated and heated flat plates

By İ. BEDİİ ÖZDEMİR AND J. H. WHITELAW
Department of Mechanical Engineering, Imperial College, Exhibition Road, London SW7 2BX, UK

(Received 13 February 1991 and in revised form 17 December 1991)

The aerodynamic and thermal aspects of the wall jet flow, formed after angled impingement of an axisymmetric jet, have been studied with emphasis on the large-scale transport of the passive scalar by the spatially coherent structures. Time-averaged and instantaneous structures of the turbulent flow were examined by visualization and local measurements of a jet arrangement with an impingement angle between the jet axis and the surface normal of 20°, a nozzle-to-plate distance to nozzle exit diameter ratio of 22, and a nozzle exit Reynolds number of 1.3×10^4.

The results show that the oblique impingement introduced vertical velocities so that boundary-layer approximations were inapplicable and led to the distribution of the time-averaged properties of the velocity and temperature field with strong azimuthal dependence, which increased gradually with angle of impingement to 40° where a sudden change of the orientation of the contours of surface pressure and temperature took place. It also led to instantaneous, spatially coherent structures which were most pronounced at an angle of 20°. These structures improved the large-scale transport of the passive scalar but, owing to the extreme regularity of their path, also led to an inactive zone near the vortex centre.

The inner region of the decelerating wall jet exhibited a momentum equilibrium layer extending to the point of radial velocity maximum and the intercept of the linear region of the semilogarithmic wall law varied in the local streamwise direction as for turbulent flows over rough walls with adverse pressure gradient. The thermal equilibrium layer had an invariant functional form but extended far beyond the point of maximum velocity.

1. Introduction

The impingement of jets on surfaces is common in nature and in engineering applications and this had led to investigations of single and multiple jets with a range of orientations to surfaces. As a consequence, there is knowledge of the time-averaged flow field such as surface pressure distribution (Taylor 1960, 1966; Foss & Kleis 1976; Foss 1979) and growth rates of the associated wall jets (Bakke 1957; Tailland & Mathieu 1967). Much attention has been given to an interesting turbulence characteristic of radial wall jets, as pointed out by Poreh, Tsuei & Cermak (1967), that turbulence intensities of radial wall jets are higher than those of boundary-layer flows. Schwarz & Cosart (1961) attributed this phenomenon to the penetration of the outer-layer turbulent fluctuations into the inner layer and concluded that the asymmetrical shape of the streamwise velocity distribution caused the minimum shear stress to occur at a location different from that of the velocity maximum. The resulting change in the structure of the inner-layer

turbulence, as shown by Bradshaw & Love (1959), involved higher skin friction coefficients and this particular characteristic of wall jets has been of interest in the study of the stagnation-zone heat transfer in the presence of impinging jets, which is known to be complex with the maximum heat flux occurring away from the geometrical impingement point and influenced by the turbulence characteristics of the jet flow, see for example Kestin & Wood (1969). In contrast to the free turbulent jet in unbounded media, the flow field of radial wall jets is dependent on the inflowing jet initial conditions even at large radial distances from the stagnation point (Poreh *et al.* 1967) and, thus, any investigation on the structure of the wall jet mean flow and related phenomena such as mass or wall heat transfer, as for example Donaldson, Snedekar & Margolis (1971), has required prior examination of the modifications to the free jet, as by Donaldson & Snedekar (1971).

Since the magnitude of velocity in the outer region of the inflowing jet does not change much as streamlines are deflected, the turbulence structure of the outer region of the wall jet is expected to correlate with that of the inflowing free jet. However, the rapid distortion in the inner part of the impingement region can be severe, and the experimental results of Gutmark, Wolfshtein & Wygnanski (1978) revealed the presence of strong spectral modifications from the inflowing jet turbulence in the region within 20% of the distance from the plate to the nozzle. They argued that turbulent energy was attenuated by viscous dissipation above a certain frequency, below which it was augmented by vortex stretching of the diverging streamlines. The boundary layer, formed when a round turbulent jet impinges at right angle on a flat plate, spreads radially so that the radial velocities decrease slowly as the boundary-layer thickness increases. Thus, analytical predictions of the general features of the mean wall flow field by simple integral momentum approaches have been possible with boundary-layer approximations, as for example Glauert (1956). It will be shown, however, that with angled impingement, azimuthal variations in the radial velocity increase rapidly as the impingement deviates from normal, and the presence of vertical velocities precludes the use of boundary-layer approximations. Also, the need for three independent variables has so far precluded the calculation of detailed results which is consistent with the difficulties in achieving grid-independent solutions for a jet in crossflow, as described in Claus & Vanka (1990).

Although there is extensive knowledge of the time-averaged flow field, a more complete description of impinging jet flows requires examination of the instantaneous flow structures. In this connection, Ho & Nosseir (1981) studied resonant interactions between downstream-convected free-jet coherent structures and upstream-propagating pressure waves generated during the impingement and identified the presence of a feedback mechanism. Didden & Ho (1985) showed that impingement of the ring vortices induced an unsteady separation of the wall jet flow and that the structure of the inner layer correlated with the outer layer and with the inflowing free-jet shear layer. In recent work with a circular water jet, Landreth & Adrian (1990) quantified the spatially coherent structure of the wall flow using particle image displacement velocimetry.

The present study was motivated, in part, by a need to provide better understanding of the consequences of the impingement of fuel sprays on the cylinders of internal-combustion engines, in particular the wall-wetting phenomenon. The situation in which the evaporation of the deposited fuel on the wall constitutes a continuous source of the passive scalar (fuel mass-concentration) for the air flow above it, was approximated by marking the flow with temperature, another passive

scalar which has the same molecular diffusion mechanism, in an experimental configuration in which the cold air impinges on a constant-flux heated wall. Thus, the present steady air jet represents an early stage in investigating the possibility of exploiting the downwash action of radial wall jets to prevent deposition of transferable quantities around the impingement point. This requires better understanding of the evolution of the time-averaged mean and turbulence velocity fields of a wall jet produced after oblique impingement and examination of instantaneous properties of the flow field. In particular, spatially coherent flow structures are important (Ottino 1989) for the kinematics of the mixing of a passive scalar, since they improve the stretching and folding of the surfaces at the material interfaces, creating more area for molecular diffusion. The results emphasize one impingement angle and one distance from the exit of the round jet to the surface. The measurements include velocity and temperature characteristics and these are related to photographs of the flow, including those of surface streaks and temperature-sensitive liquid crystals. The emphasis is on the structure of the flow and on the azimuthal variations associated with radial wall jets.

2. Flow configuration, measurement techniques and accuracy

The jet emerged from a convergent nozzle of 10 mm diameter, d_E, with a bulk velocity $U_E = 20$ m/s and corresponding Reynolds number of 1.3×10^4. Compressed air at 23 °C was passed through a pressure regulator, a rotameter and a mixer arrangement where particles could be added to the nozzle which had a contraction ratio of 16. The profile of mean velocity at the exit had turbulent shear layers with thickness, corresponding to the location at which the velocity reached 0.99 of the centreline value, of $0.037d_E$. The r.m.s. of velocity fluctuations at the centreline, normalized by the mean velocity, was 0.01. The jet was arranged so that the centre of its exit plane was 220 mm from a flat surface ($H/d_E = 22$) with dimensions $600 \times 600 \times 15$ mm and the angle of the jet axis to the surface normal could be varied from 0 to 40°. Plates of different material were used depending upon the measurements required.

The general arrangement of the jet and surface is shown in figure 1 together with the cylindrical coordinate system which had its origin at the intersection of the axis of the jet with the surface. The figure also shows the plane of incidence which was observed visually and subsequently photographed with the assistance of a sheet of laser light, generated by an Argon-ion laser (Spectra Physics Model 164) operated at 514.5 nm and 700 mW and expanded by a cylindrical lens of 5 mm focal length and a plano-convex lens of 300 mm focal length, and neutrally buoyant microballoons (75 μm average diameter) which were added in the mixing chamber. A 35 mm single-lens reflex camera with a 55 mm objective lens was focused on the 2 mm thick laser sheet with photographs recorded on Kodak Tmax P3200 film and push-processed at 6400 ASA. For these experiments, a glass plate of good surface quality was used as the surface material to minimize multiple reflections, and the experiments were carried out in a darkened room. The exposure time depended on the jet velocity and the region of flow being photographed.

The variation of wall shear stress was observed in terms of streaks of pigmented oil which was sprayed uniformly on the glass plate and subjected to the jet flow seeded with atomized kerosene. The emulsion of titanium dioxide and kerosene was arranged after a number of experiments, and the photographs of figure 2 were taken when the emulsion had dried.

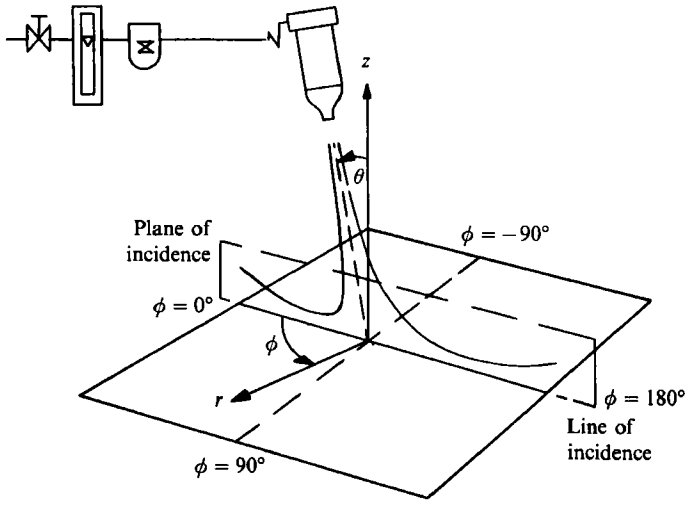

FIGURE 1. General arrangement of the experimental set-up.

Surface pressures were measured within a half-circle of 80 mm radius through 0.4 mm diameter holes in a Plexiglas plate. The holes were arranged carefully so as to be free from surface imperfections and an inclined manometer (Combustion Instruments, Combist Micromanometer) allowed resolution within 2 μm of water. The pressure measurements varied from static values at large distances from the impingement location to total-head pressures at impingement. The plate orientation was readily changed to allow measurement within a full circle.

The radial and vertical components of mean velocity, U and V, the intensity of the corresponding fluctuations, $\overline{u^2}$ and $\overline{v^2}$, and higher-order moments were measured with a laser velocimeter and spectral information was obtained with a hot-wire anemometer. The velocimeter comprised a 5 mW helium-neon laser, with transmitting and collection optical components (Dantec Model LDA04) and providing Doppler signals from droplets of vegetable oil (diameter $d_d < 2$ μm) generated by an air-blast atomizer. The forward-scattered light was, in general, collected within a solid angle with 10° of half-cone angle to the axis of the transmitted laser beam to ensure high signal-to-noise ratio. With effective frequency shifts in the range of 10 kHz and 9 MHz, the signals were processed by a counter described by Founti & Laker (1981) interfaced to a microcomputer (Apple II). All velocity values were based on more than 1900 individual measurements and the only other important source of uncertainty stemmed from gradient broadening (Kreid 1974) which was always less than 0.67% of the mean value with this maximum value confined to the near-wall region. As a consequence, the average uncertainties in mean and r.m.s. values of velocity fluctuations did not exceed 2 and 5% of the local values respectively.

One-dimensional spectral measurements were obtained from a 5 μm diameter and 1.25 mm long platinum-plated tungsten wire sensor (DISA 55P11) and instrumentation comprising a constant-temperature hot-wire anemometer (DISA 55M01), a linearizer (DISA 55D10) and a spectrum analyser (Spectral Dynamics, Model SD340) with a frequency resolution of 0.25 Hz in a range of 100 Hz.

The variation of surface temperature was observed on photographs in terms of a sheet of temperature-sensitive liquid crystal material (Liquid Crystal Devices Ltd) with recognizable contrast within 1 °C. The sheets of liquid-crystal material were

placed on a plate of Duralumin, subjected to heat transfer from a heating blanket with a maximum power output of 800 W. The blanket was sandwiched between the Duralumin plate and a wooden plate of thickness 50 mm which ensured uniform temperature at the surface of the Duralumin plate. The plate was raised in temperature to around 39 °C, with the corresponding surface heat flux $\dot{Q}''_{\mathrm{w}}$ of 215 W/m^2, the jet-flow started and the surface of the liquid crystals observed after the steady state had been achieved, in less than 20 min. Ten copper-constantan thermocouples were embedded 1.5 mm below the upper surface of the Duralumin plate and confirmed the constant temperature of the plate to ± 0.5 °C, in the absence of the jet.

The mean and r.m.s. values of the temperature of the air above the impingement plate, which was heated for this experiment up to around 100 °C with the corresponding surface heat flux of 954 W/m^2, were measured with the same wire sensor (DISA 55P11), but operated as a cold wire at a constant current so to provide sensitivity to temperature and negligible sensitivity to velocity. The instrumentation comprised a constant-current circuit and a signal conditioning unit with 20 mV peak-to-peak noise. The uncertainty in the measurement of temperature was estimated to be less than 0.5 °C.

3. Results and discussion

3.1. *Presentation of results*

The maximum mean value of the radial component of the velocity, U_{M}, was used as the scaling parameter for the velocity of the wall flow at each measuring radial position because, as shown later, it characterized the decay of the mean radial velocity as well as the dividing surface (Foss 1979) between the positive and negative mean vorticity parallel to the plate ($\omega_\phi = \partial U/\partial z - \partial V/\partial r$). The half-velocity thickness of the same component normal to the plate, $z_{0.5}$, represented the growth of the inner wall-bounded and outer free shear layers, and thus was used to normalize the wall distance, z, as the lengthscale of the corresponding profile. Westley, Woolley & Brosseau (1972) suggested that major features of the wall jet formed after oblique impingement can be transformed to non-dimensional form by the use of nozzle-to-plate distance, H, and angle of impingement, θ, and thus, the radial distance, r, was rendered dimensionless in terms of a more global parameter, the projected jet diameter that would exist at the stagnation region if the plate were removed, D. This was approximated using a power law for the round turbulent jet which, for a jet inclined by 20°, yields

$$D = \frac{H}{\cos\theta} = 234 \text{ mm}.$$

The global velocity scaling, U_{c}, is calculated similarly as

$$U_{\mathrm{c}} = \frac{U_{\mathrm{E}} d_{\mathrm{E}}}{H} = 0.909 \text{ m/s},$$

and used to normalize the variation of the radial velocity maximum along the line of incidence.

The downstream evolution of the velocity field of the wall flow was investigated radially from $r/D = 0.043$ to 0.812 in forward ($\phi = 180°$), backward ($\phi = 0$) and side directions ($\phi = 90°$). Radial distances were $0.128D$ apart except in the backward

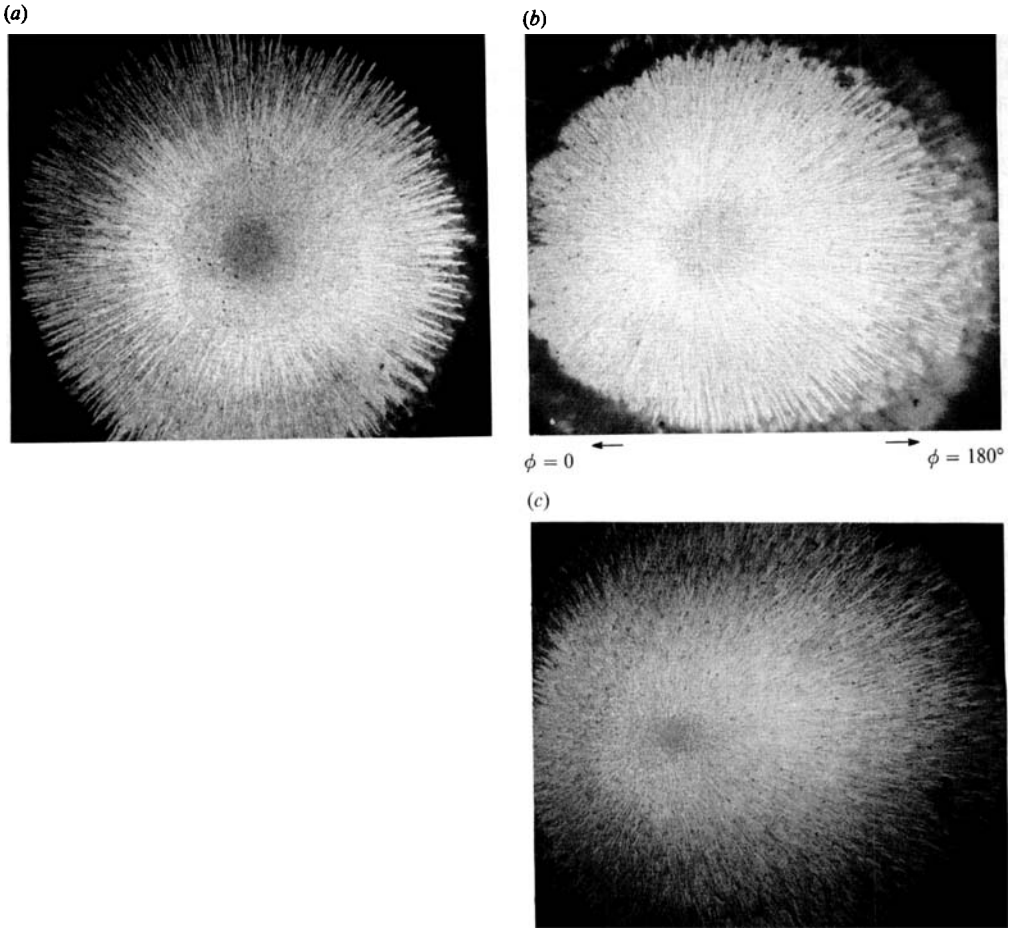

FIGURE 2. Surface visualization for impingement angles of (a) $\theta = 0$, (b) $\theta = 20°$ and (c) $\theta = 40°$: $Re_E = 1.3 \times 10^4$, $H/d_E = 22$.

direction where between $r/D = 0.043$ to 0.171 two more stations were included, and the velocimeter was traversed normal to the plate in steps of 0.5 mm from the wall to $z = 4$ mm with increasingly larger intervals thereafter.

The characteristic lengthscale for the temperature profiles was selected as the penetration depth of the thermal activity, z_P, the wall distance at which the temperature r.m.s. attained half the difference between its maximum and the ambient level. The characteristic temperature, T_c, of a given radial position was the difference between the wall temperature and the time-averaged ambient temperature: $T_c = T_w - T_A$.

The temperature field of the wall flow was investigated along the line of incidence at the same radial positions as the velocity profiles. The cold wire was traversed normal to the plate in steps of 0.5 mm for the first eight points and larger steps afterwards according to the evolution of the profiles. Because the profiles developed similarly in the backward and forward directions, no attempt was made to investigate the evolution along the side direction.

In the following paragraphs, the aerodynamic results are presented followed by those for heat transfer and, in each case, photographic observations are introduced

first so as to provide a general view of the flow. Surface visualization and pressure measurements are presented for a number of angles to the surface and detailed velocity and temperature measurements correspond to the 20° angle.

3.2. *Visualization*

Figure 2 shows typical photographs of the pigmented-oil surface for three angles. Normal impingement results in a symmetrical wall flow pattern with no streaks in the immediate vicinity of impingement due to the high local value of wall shear stress which reduces with radius and leads to a value insufficient to move the oil at the outer extent of the streaks. The distance between streaks increases with radius as would be expected from mass continuity of the radial flow since the entrainment is too small to be important to the dynamics of the spreading. As the impingement angle increases, the impingement region with high wall stress and the so-called stagnation bubble decrease in area and the radial symmetry of the stagnation bubble and the surrounding oil-streak pattern becomes increasingly elliptical. These observations are consistent with those of Donaldson & Snedekar (1971) and Westley *et al.* (1972). The forward direction of the flow ($90° < \phi < 270°$) is characterized by the larger distance from the geometrical impingement point ($r = 0$) to the end of the oil streaks, corresponding to the larger effective free-stream velocity and wall shear stress.

The photographs of figure 3 correspond to the laser light sheet located in the plane of incidence and were obtained in three parts, two corresponding to near and far fields in the plane $\phi = 0$ (*b* and *a*), and one corresponding to the near field in the plane $\phi = 180°$ (*c*). The diagrammatic interpretation of the streaks caused by the microballoons indicates very different flow structures in the two directions. The flow pattern in the $\phi = 0$ plane has neither a well-defined wall jet nor a single stationary vortex in contrast to that observed in the $\phi = 180°$ plane. In the former case, an array of vortices is formed just downstream of the impingement point as the outer streamlines roll up and is convected by the radial mean flow. The vortices grow with distance and remain discrete further downstream. The boundary layer has formed wavy streamlines between the vortices and the wall with corresponding variations in wall shear occurring in distance and time. The downstream-moving unsteady separation discussed by Didden & Ho (1985), in relation to the appearance of a counter-rotating vortex under wavy streamlines, is not clear in photograph (*b*), but the incipient separation shown in photograph (*a*) is probably related to the growth of a moving vortex in the vicinity of the wall.

Within the plane of $\phi = 180°$, a wall jet exists with large external flow recirculation, and the intermittency of the external region of the shear layer is similar to that observed in boundary layers, for example, those of Head & Bandyopadhyay (1981). The downstream extent of the large vortex is not evident in figure 3 and additional photographs confirmed its existence at $r/D = 0.812$ where the wall flow still appeared to be attached.

The different types of flow observed within the plane of incidence on both ($\phi = 0$ and 180°) sides of the geometrical impingement point must be related azimuthally so that they form two different azimuthal sectors of the same fanwise-spreading wall flow. This is only possible if the wall flow field comprises three-dimensional, concentric, toroidal vortex tubes around the geometrical impingement point which merge azimuthally and become circumferentially tangential at $\phi = 180°$, see figure 3(*e*), so that those vortices which seem discrete in the $\phi = 0$ plane are perceived as a single stationary large structure in the $\phi = 180°$ plane.

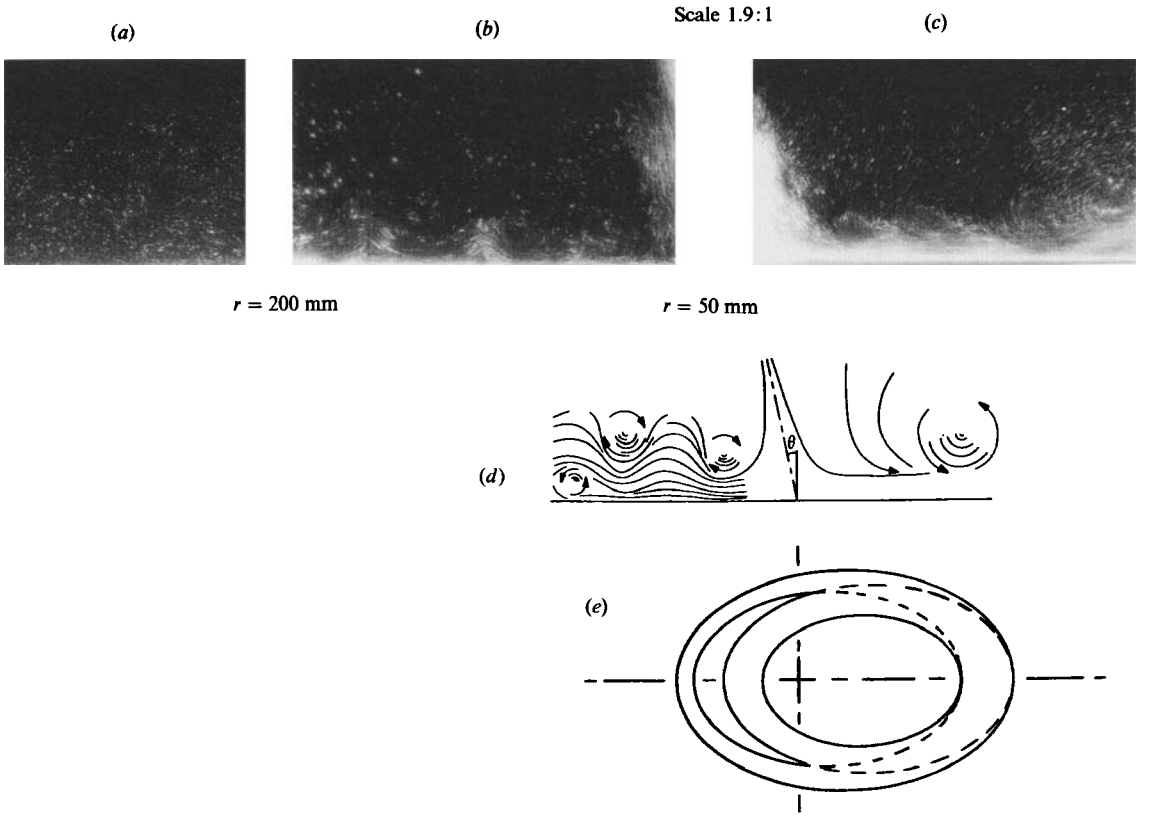

FIGURE 3. Visualization of the plane of incidence: $Re_E = 1.3 \times 10^4$, $H/d_E = 22$: (*a*) far downstream view, $\phi = 0$; (*b*) near-field view, $\phi = 0$; (*c*) near-field view, $\phi = 180°$; (*d*) schematic of the flow within the plane of incidence; (*e*) schematic of the presumed toroids seen from the top.

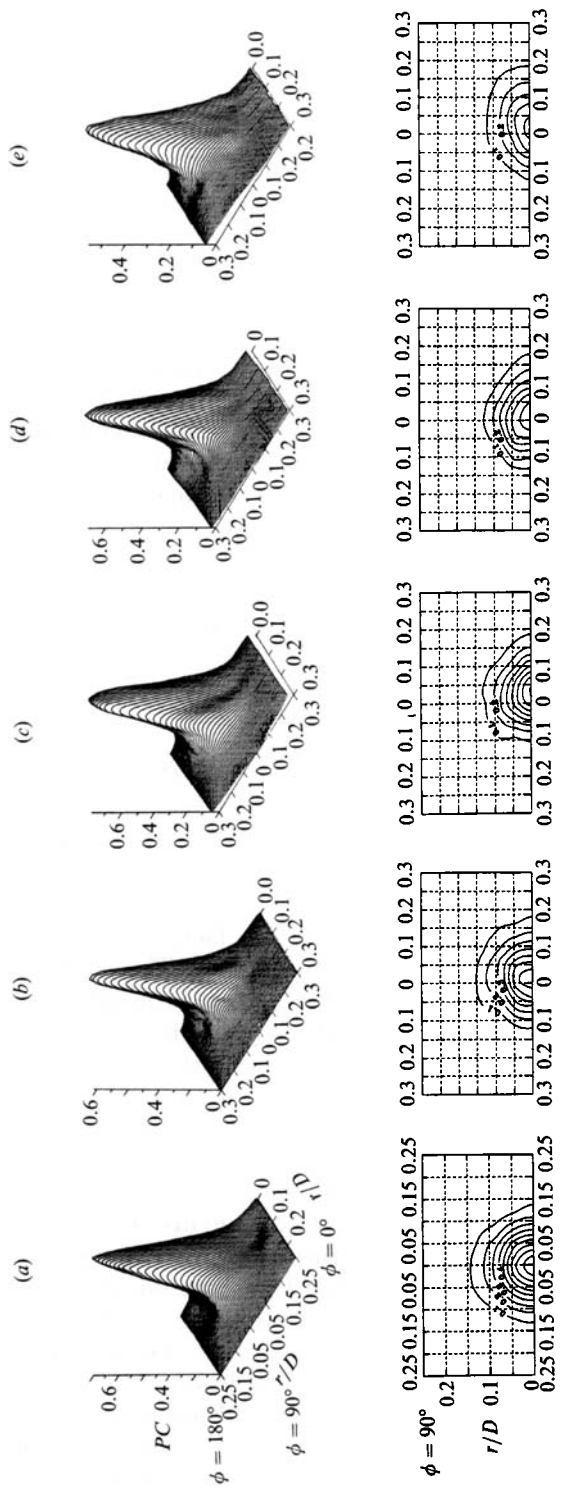

FIGURE 4. Surface pressure coefficients: (*a*) $\theta = 0$, (*b*) $\theta = 10°$, (*c*) $\theta = 20°$, (*d*) $\theta = 30°$ (*e*) $\theta = 40°$. $Re_E = 1.3 \times 10^4$, $H/d_E = 22$.

θ (deg.)	0	10	20	30	40
$\frac{P_M - P_A}{\frac{1}{2}\rho U_E^2} \times 10^3$	11.3	9.1	8.3	7.4	6.0

TABLE 1. Variation of maximum surface pressure

It is possible that the organized structures observed in the $\phi = 0$ plane stem from coherent structures alrcady present in the free shear layer of the inflowing jet but the dimensions of the fluid patches on the jet periphery before the impingement and those on the wall jet after the impingement are different. Analysis of the photographs of the other jet arrangements has led to the conclusion that the moving vortices of the wall jet cannot be obtained by a radial transformation of ring vortices of inflowing jet, but are a consequence of multiple interaction of two or more ring vortices on the jet periphery, rather like the vortex-interaction mechanism suggested by Ho & Nosseir (1980). This argument is consistent with that of Gutmark *et al.* (1978), in relation to the normal impingement of their plane jet.

3.3. *Surface pressure*

Measured values of surface pressure are provided in figure 4 in the form of three-dimensional diagrams and contours of the pressure coefficient,

$$PC = \frac{P - P_A}{(P_M - P_A)|_{\theta=0}}, \tag{1}$$

where P_A is the time-averaged ambient pressure and P_M the maximum time-averaged surface pressure. The non-dimensional maximum gauge pressure, $(P_M - P_A)/(\frac{1}{2}\rho U_E^2)$, varied with impingement angle as in table 1. It is evident that the surface pressure in the immediate vicinity of impingement point tends rapidly to the atmospheric value so that the diagrams encompass a small region of the wall flow field. The very rapid decrease in pressure coefficient from the location of $r = 0$ also indicates the equivalent rapid deflection of the jet streamlines. The single-peak feature of the three-dimensional diagrams of pressure coefficient is consistent with that of Westley *et al.* (1972) for a non-dimensional nozzle-to-plate distance, $H/d_E = 12$, but differs from their oblique cases with smaller H/d_E due to the presence of a potential core in the inflowing jet just upstream of the plate. It is interesting to note that the potential core causes a two-peaked stagnation ridge only when impingement deviates from normal.

The contour plot of constant pressure coefficient is symmetrical with normal impingement and assumes the egg shapes of figure 4 as the angle is increased. However, there is a distinct change in the orientation of the contours with $\theta = 40°$, for which the egg shape is reversed so that the blunt side occurs on the $\phi = 180°$ line and is located away from the impingement point ($r = 0$). The shapes of the contours for $\theta = 40°$ impingement are qualitatively similar to those reported by Foss & Kleis (1976) for an inclination of $\theta = 81°$ and that of Foss (1979) for $\theta = 45°$. As the angle of impingement is increased to 40°, the jet–wall interaction is reduced so that the maximum of the stagnation pressure ridge drops to almost half the value of normal impingement. In these shallow-angle impingements, the free jet is deflected from its original direction so that the small pressure built-up in the impingement region cannot deflect the streamlines in a direction opposite to the direction of the inflowing

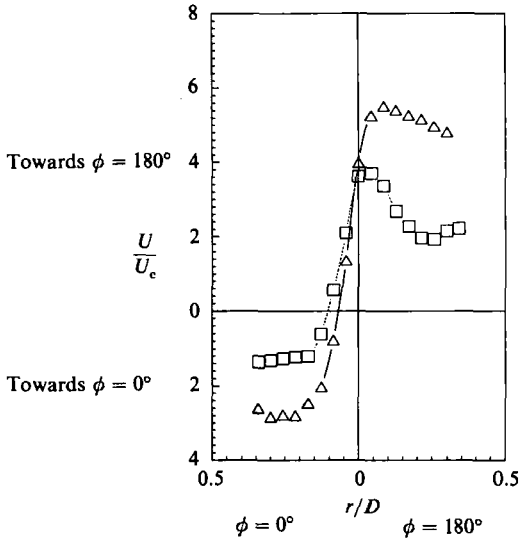

FIGURE 5. Details of the variation of the radial mean velocity in the impingement region along the line of impingement: △, $z = 5$ mm; □, $z = 10$ mm.

jet and large azimuthal variations were introduced to the fanwise spreading of the wall flow. As shown in §3.4, the wall heat transfer follows a similar trend, exhibiting strong azimuthal variations with $\theta = 40°$. It is concluded that the orientation of the jet with respect to the plate determines the flow characteristics and wall heat transfer, and the consequences of impingement with $\theta \geqslant 40°$ should be considered different from those with smaller angles.

3.4. *Velocity field*

In order to identify the virtual origin of the wall spreading, the radial component of mean velocity, U, was examined within the impingement region along the line of incidence at distances from the wall, $z = 5$ and 10 mm. Figure 5 indicates that, with the cylindrical coordinate system centred at the geometrical impingement point, the inflowing jet flow was deflected in the $\phi = 0$ and 180° directions so that the virtual origin was located along the $\phi = 0$ line and the flow was directed radially inwards at small radial distances between $r/D = 0$ and the virtual origin. The locus of the zero radial velocity occurs at both wall distances on the line of impingement and towards the $\phi = 0$ line rather than at $r/D = 0$ where the radial velocity is around $4U_c$ and directed towards $\phi = 180°$. The radial velocity subsequently increases to a maximum which is larger close to the wall and then decays. The maximum velocities are greatest on the $\phi = 0$ side.

The profiles of U-velocity, figure 6, show the development of the wall jet which, in the three directions, asymptotes to a profile described by

$$\frac{U}{U_M} = \frac{(z/z_{0.5})^{\eta-1}}{\left(\frac{\eta-1}{\eta}\right)^{\eta-1/\eta}(s\sqrt{2})^{\eta-1}} \exp\left\{-\left(\frac{z/z_{0.5}}{s\sqrt{2}}\right)^{\eta} + \frac{\eta-1}{\eta}\right\}, \tag{2}$$

with η and s the form and scale parameters of a Weibull distribution (Schmidt &

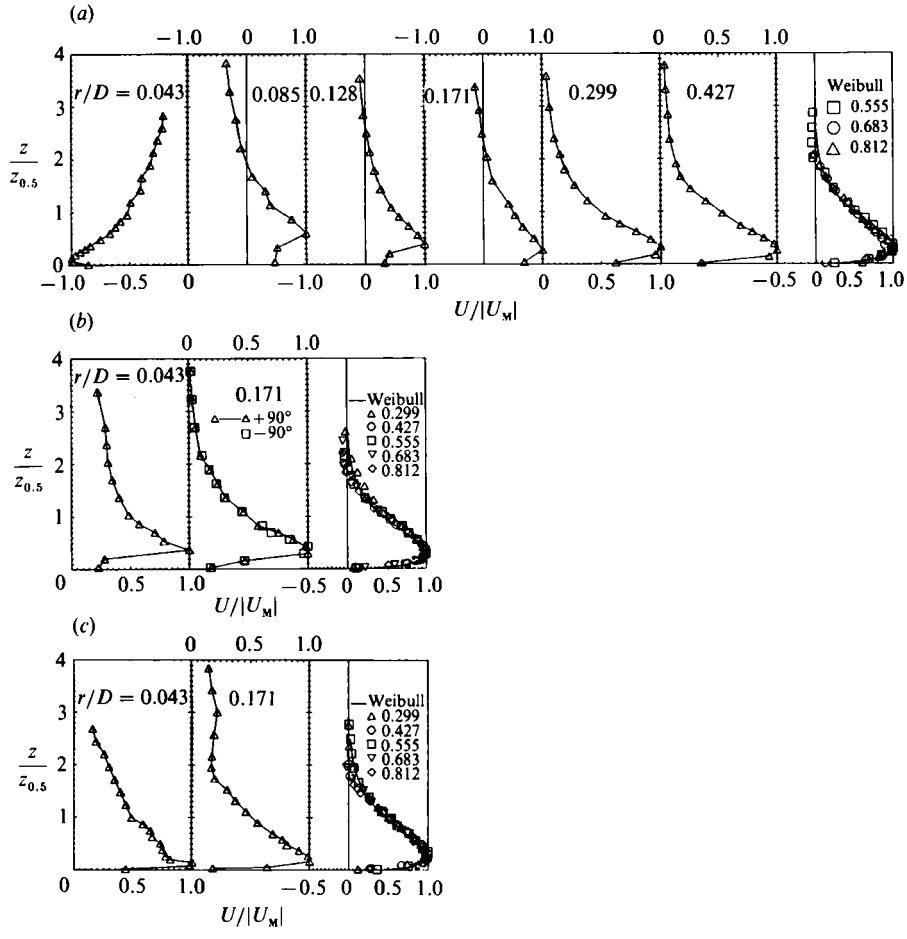

FIGURE 6. Development of the mean radial velocity profiles along (*a*) $\phi = 0$ line, (*b*) $\phi = 90°$ line, (*c*) $\phi = 180°$ line. $Re_E = 1.3 \times 10^4$, $H/d_E = 22$, $\theta = 20°$.

ϕ (deg.)	0	90	180
η	1.42	1.38	1.32
s	0.54	0.52	0.54

TABLE 2. Variation of η and s

Tondl 1986, p. 328), and varied azimuthally as given in table 2. For $\phi = 90°$ and 180°, the profiles achieve their similar form at $r/D = 0.299$, much smaller than the value of $r/D = 0.555$ for $\phi = 0$. For $\phi = 0$, radially outwards flow with always positive velocities is achieved only at $r/D = 0.299$ and the effect of the inflexion point, in evidence at the radial positions $r/D = 0.085$ and 0.128 at around $z/z_{0.5} = 0.4$, disappears completely only at $r/D = 0.555$. The inflexion point is also observed along the $\phi = 90°$ line in the profiles at $r/D = 0.043$ and 0.171. It is apparent that the suggested distribution represents the global features of the profile, such as the location of the maximum and outer inflexion point, but is not a proper approximation in the immediate vicinity of the wall, giving an infinite wall shear stress. This is consistent with the difficulties in modelling the inner equilibrium layer with the

scales based on the outer layer, when the velocity maximum is close to the wall. A momentum equilibrium layer was defined by the semilogarithmic relation,

$$\frac{U}{U_\tau} = \frac{1}{\kappa_M} \ln\left(\frac{z U_\tau}{\nu}\right) + A, \tag{3}$$

where U_τ is the wall friction velocity, κ_M the Kármán constant for momentum diffusion and ν the kinematic viscosity of air. This layer was investigated in the three directions ($\phi = 0$, 90°, and 180°) with the last three profiles plotted in terms of wall variables, and the results of figure 7(*a*) indicate that the linear region of each profile extends well clear of the wall up to the point of velocity maximum but with a variable intercept. It appears that the momentum equilibrium layer constitutes a considerable part of the inner boundary layer, which contradicts the requirement (Townsend 1976) that its thickness should be a small fraction of the total width of the turbulent flow, even though there are counter arguments (Hinze 1959). If the outer edge of the momentum equilibrium layer is attached to the point of radial velocity maximum, which is very close to the wall, it can be concluded that this maximum, U_M, should be the velocity scale to make the lines coincident. This means that the intercept, A, in (3) is not an invariant but is associated with a deviation function of the local dimensionless velocity, U_M/U_τ, i.e.

$$A = g(U_M/U_\tau),$$

where the functional form of g will be determined semi-empirically. Three linear relations, figure 7(*b*), seem to hold for each direction with small but systematic azimuthal departures and, therefore, a single relation of the form

$$A = 1.292(U_M/U_\tau) - 6.2 \tag{4}$$

approximates the trends for the three directions. When the first term on the right-hand side of (4), a profile-shift parameter, is subtracted from the left-hand side of (3), the profiles of figure 7(*c*) have a range which exhibits the characteristics of an equilibrium layer and extends to the location of velocity maximum. The systematic variation of the intercept, A, with ϕ, figure 7(*b*), agrees well with the streamwise development of the radial flow in the three directions, so that A has the largest slope and dependence on the parameter, U_M/U_τ, along the $\phi = 0$ line where the flow development was slow, with the radial velocity profiles achieving their similar form at the farthest radial distance, $r/D = 0.555$. The effect of streamwise flow development on the law of the wall is similar to that reported by Perry, Schofield & Joubert (1969) for turbulent flows over the rough surfaces with adverse pressure gradient.

The decay of the radial velocity along the wall jet, figure 8(*a*), is represented by

$$U_M = C_1/r^n, \tag{5}$$

where C_1 was found to be 0.095 and 0.269 and the exponent n to be 1.459 and 1.057 for $\phi = 0$ and 180°, respectively. For a symmetrical radial wall jet, values of the exponent were reported to be 1.12, 1.1, and 1.14 by Bakke (1957), Poreh *et al.* (1967) and Glauert (1956), respectively and the present results indicate that n, and so the decay of radial spreading, depend on impingement angle and that the decay was faster than that of a free turbulent round jet ($n = 1$, Abramovich 1963, p. 199) along the $\phi = 0$ line, and close to that of a free jet along the $\phi = 180°$ line.

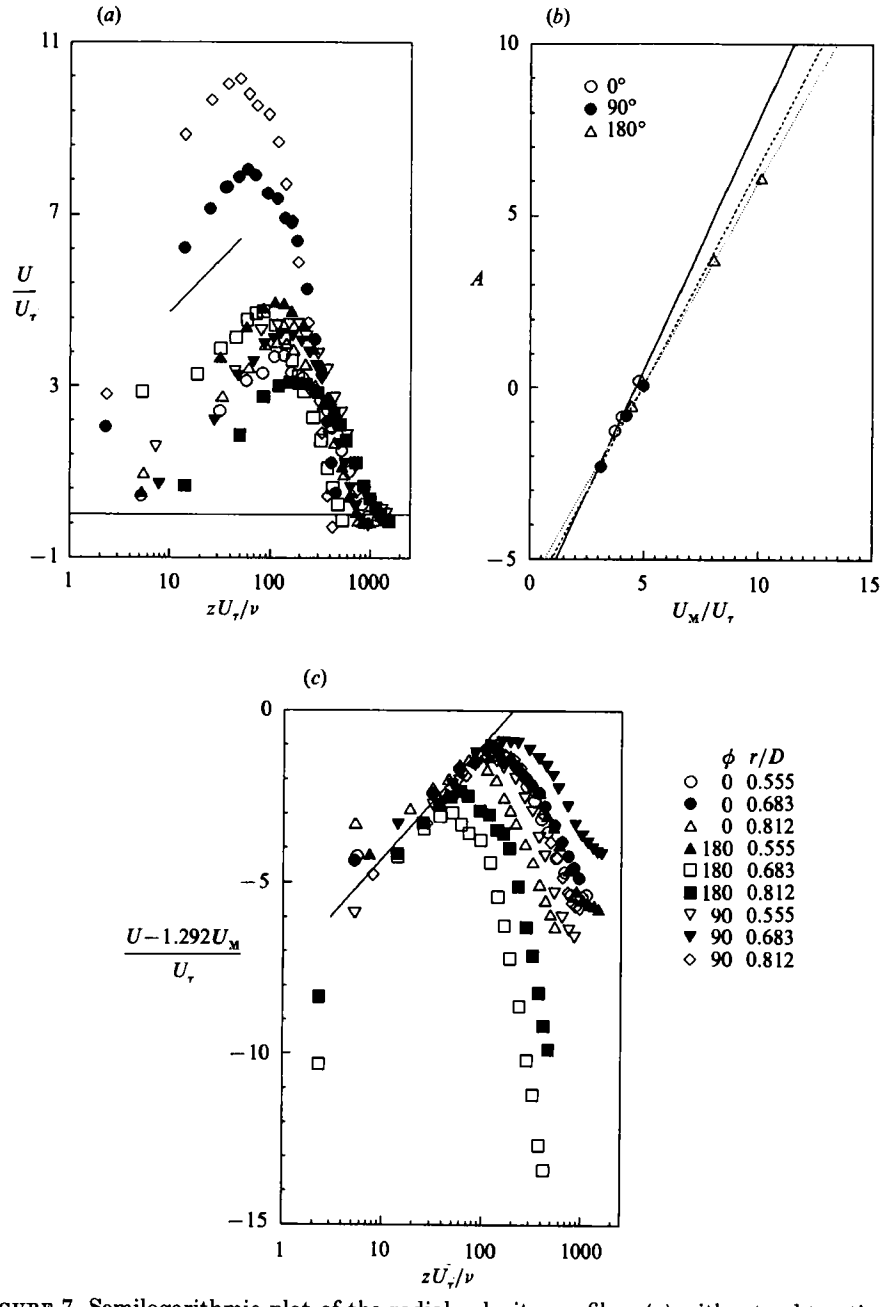

FIGURE 7. Semilogarithmic plot of the radial velocity profiles: (*a*) without subtracting the profile-shift parameter, (*b*) deviation function, (*c*) with subtracting the profile-shift parameter.

The growth of the wall jet in terms of half-velocity thickness, $z_{0.5}$, figure 8(*b*), can be approximated by

$$z_{0.5} = C_2 r^m \tag{6}$$

where C_2 was 0.242 and 0.138, and the exponent m was 1.156 and 1.385 for $\phi = 0$ and 180°, respectively, indicating a much faster growth, especially along $\phi = 180°$ line, than for a symmetrical radial wall jet, which was found in Bakke (1957) and Poreh *et al.* (1967) to be 0.94 and 0.9, respectively.

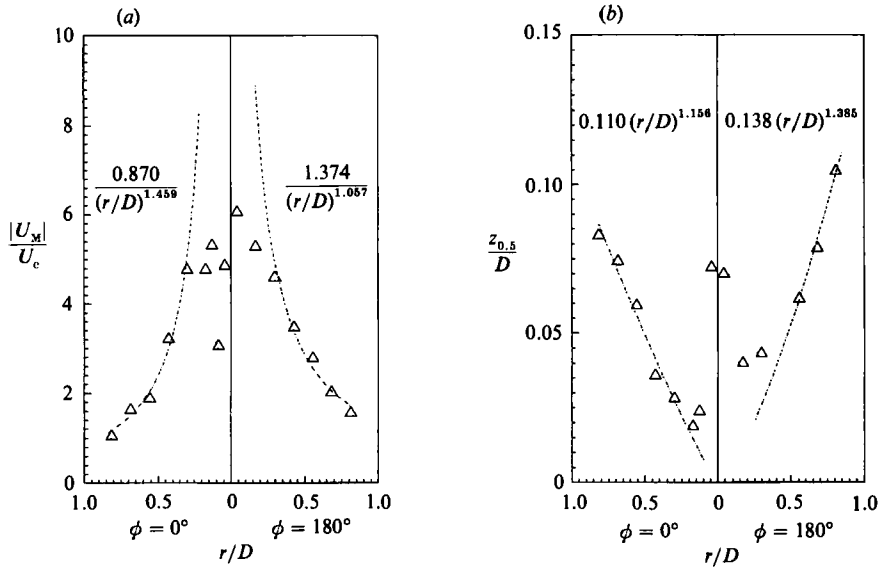

FIGURE 8. (*a*) Decay of the maximum of the radial mean velocity. (*b*) Growth of the wall jet thickness in terms of half-velocity thickness.

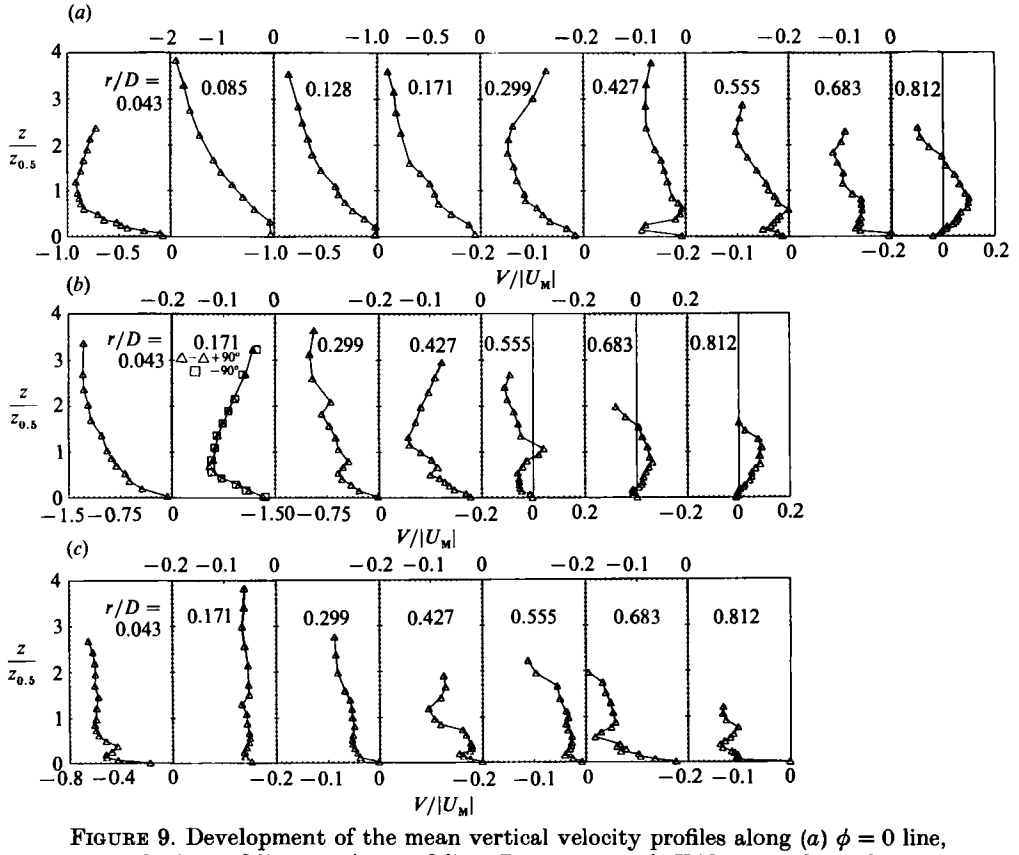

FIGURE 9. Development of the mean vertical velocity profiles along (*a*) $\phi = 0$ line, (*b*) $\phi = 90°$ line, (*c*) $\phi = 180°$ line. $Re_E = 1.3 \times 10^4$, $H/d_E = 22$, $\theta = 20°$.

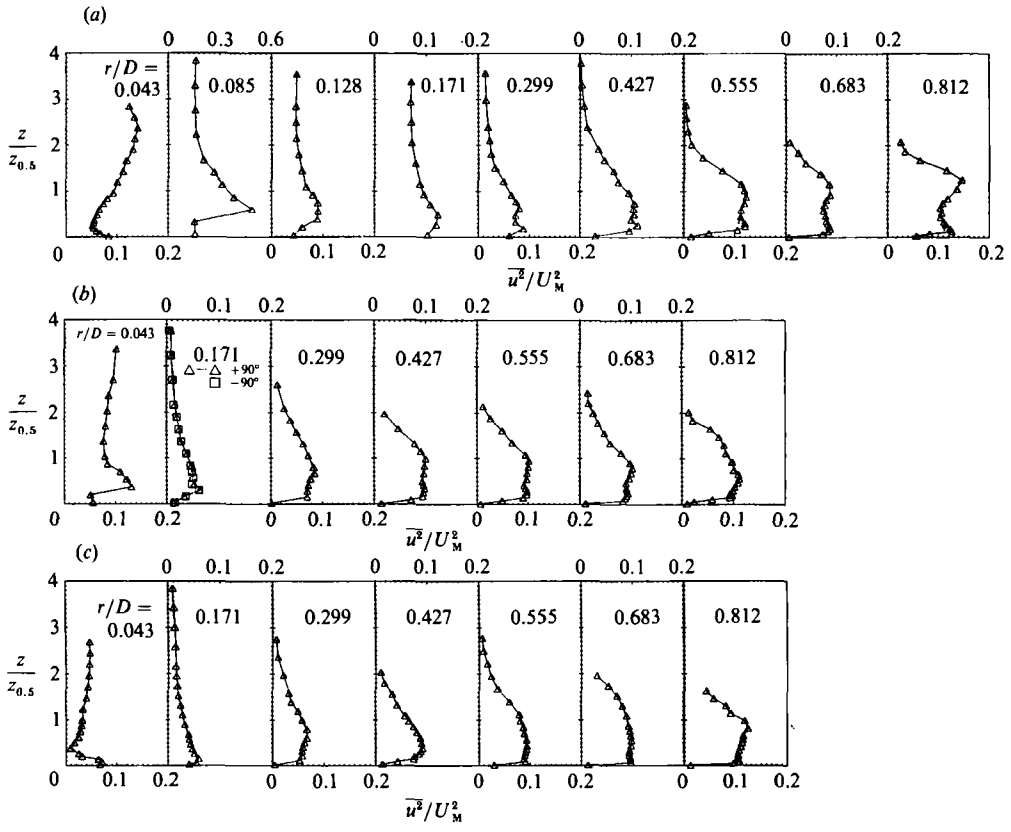

FIGURE 10. Development of the radial fluctuation intensity profiles along (*a*) $\phi = 0$ line, (*b*) $\phi = 90°$ line, (*c*) $\phi = 180°$ line. $Re_E = 1.3 \times 10^4$, $H/d_E = 22$, $\theta = 20°$.

As seen in figure 9 the velocities normal to the wall are larger with the present angled impingement than those in the normal impingement cases reported in the literature (Didden & Ho 1985; Landreth & Adrian 1990), where the boundary-layer approximation might be appropriate, and this feature increases entrainment of the second kind, as defined by Perry, Lim & Chong (1980), due to flow spiralling towards the centres of the vortices. In contrast to the profiles along the $\phi = 180°$ line, where there is strong vertical flow towards the plate throughout the wall jet, the profiles along the $\phi = 0$ and 90° lines develop local vertical flow reversals at large radial distances, which was also reported by Landreth & Adrian (1990) at $r/D = 2.2$ for their round turbulent water jet of Reynolds number 6564.

The intensity of radial velocity fluctuations, figure 10, exhibits an interesting development along the $\phi = 0$ line with two distinct peaks in the profile from $r/D = 0.299$ and thereafter; they also exist, but are less well defined for $\phi = 90°$ and 180°. This two-peak feature was also reported by Tsuji, Morikawa & Sakou (1977*a*), and Tsuji *et al.* (1977*b*) in their measurements of plane and radial jets but, in the two-dimensional wall jet of Irwin (1973), the peak in the inner layer was weak and similar to those for $\phi = 90°$ and 180°. There is also theoretical evidence, based on the stability analyses of Özdemir (1992) and Mele *et al.* (1986), that the mean radial velocity profile can cause large-scale disturbances with greater magnitude in the outer layer and small-scale disturbances close to the wall.

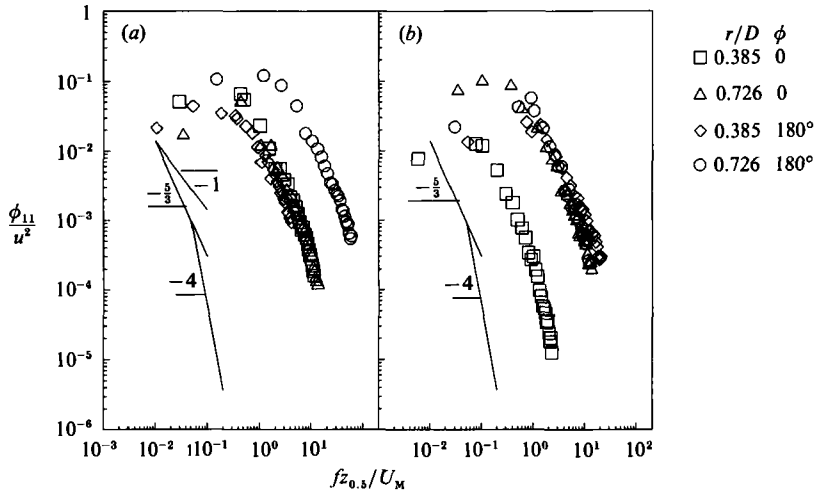

FIGURE 11. One-dimensional spectral distribution of the radial fluctuation component, u; (a) in the inner layer, $z = 2$ mm, (b) in the outer layer, $z = 32$ mm and 22 mm for $\phi = 0$ and 180°: $Re_E = 1.3 \times 10^4$, $H/d_E = 22$, $\theta = 20°$.

A representative selection of one-dimensional spectral distributions of the radial fluctuation component in the inner and outer layers, non-dimensionalized by $\overline{u^2}$, is given in figure 11 (a, b). In both cases, there is an extensive range where Kolmogorov's $-\frac{5}{3}$ decay law is closely followed for moderate values of Strouhal number, $St = fz_{0.5}/U_M$, so that eddy transfer dominates viscous dissipation and interaction with the mean flow. Isotropy is evident despite the large structures and asymmetric stretching due to the oblique impingement, and the anisotropy, which might be caused by distortion of the large structures by the wall, has been avoided by the unrestricted upper boundary which allows the structures to arrange themselves without deformation. The curves deviate markedly from the -7 decay law of isotropic turbulence (Hinze 1959) for large values of St where the slope of the decay is close to -4. It may also be noted that the curves for the points very close to the wall have milder slope in the low-Strouhal-number range than those for the points in the outer free shear layer, which implies that the spectrum function varies nearly with the slope of -1 only close to the wall, indicating strong interaction between the mean flow and the turbulence in the immediate vicinity of the wall and not in the free shear layer. Even though the spectral distributions are plotted against Strouhal number they do not collapse to a single curve, indicating that turbulent similarity does not exist throughout the wall flow.

The possibility that the vortices in the $\phi = 0$ plane had their origin in the inflowing jet and subsequently evolved in the wall flow was investigated in the outer free shear layer at $z = 25$ mm and in the inner wall-bounded shear layer at $z = 2.5$ mm at radial positions $r/D = 0.427$, 0.555, 0.683 and 0.812. The sequence of figure 12 (a) shows the spectrum of hot-wire signals obtained at $z = 25$ mm and reveals that several low-energy discrete frequencies are present, as would be expected from investigations of mixing layers such as those of Husain & Hussain (1979) and Zaman & Hussain (1980), but only one frequency dominates at each position. Further downstream, the exact location of the dominant frequency drifts towards lower frequencies; it starts with a value of 6 Hz at $r/D = 0.427$ and falls to 5.25, 5 and eventually to 3.25 Hz at $r/D = 0.812$, and this is consistent with the growth of the wavelength, λ, of the

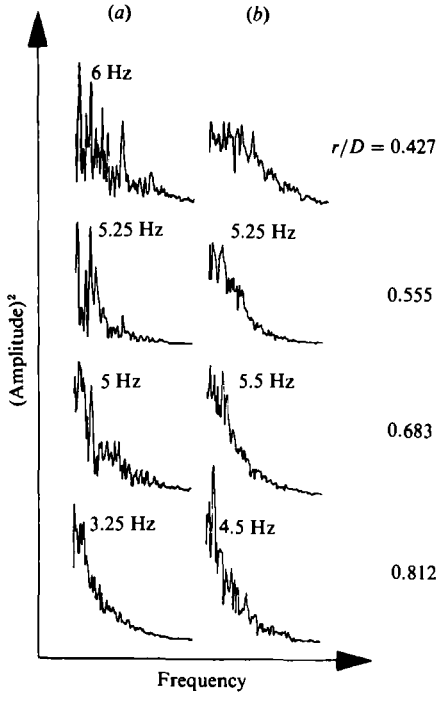

FIGURE 12. Spatial evolution of the low end of the one-dimensional spectrum of u (the unit of the y-axis is arbitrary): (a) $z = 25$ mm; (b) $z = 2.5$ mm: $Re_E = 1.3 \times 10^4$, $H/d_E = 22$, $\theta = 20°$.

periodic component of the signal in the downstream direction. The results of the stability analysis of Özdemir (1992) on the same flow also agree with these, revealing that the least attenuation of the decaying waves at $r/D = 0.812$ occurs at 3.1 Hz. From figure 3(*b*), the size of the vortex passing the radial positions $r/D = 0.427$ and 0.555 was estimated as $\lambda = 31$ mm and 38 mm which gives local convection speeds, $U_{TR} = f\lambda$, of 0.187 m/s and 0.204 m/s, respectively. Non-dimensionalizing these results with the local radial velocity at the probe location led to an almost constant convection speed of around 0.92. Considering the decay of the maximum radial velocity from 2.952 to 1.744 m/s, it is then clear that the vortices accelerate with respect to mean flow field between these two stations and this may enhance passive-scalar mixing by the vortical structures. It is not possible to estimate the size of the vortices from figure 3(*b*) beyond $r/D = 0.555$, and further conclusions about the mechanisms leading to vortex breakdown are difficult. The sequence of figure 12(*b*) shows the corresponding spatial evolution of the spectrum at $z = 2.5$ mm and reveals again a dominant frequency of about 5 Hz due to the counter-rotating vortex in the inner layer. Since this vortex moved between two outer-layer vortices, its growth was partially restricted and, as a consequence, the change in the corresponding wavelength and so the frequency was too small to be detected.

The vertical fluctuation intensity, $\overline{v^2}/U_M^2$, shown in figure 13, develops a single peak at large radii and at a distance from the wall which coincides with the position of the velocity defect in the mean vertical profile, caused a local vertical flow reversal along the $\phi = 0$ and 90° lines.

It has been argued by Townsend (1976) that the joint-normal distribution of spatially homogeneous turbulent flows is distorted by any inhomogeneity, and the resulting departures are realized by non-zero odd moments and abnormally large

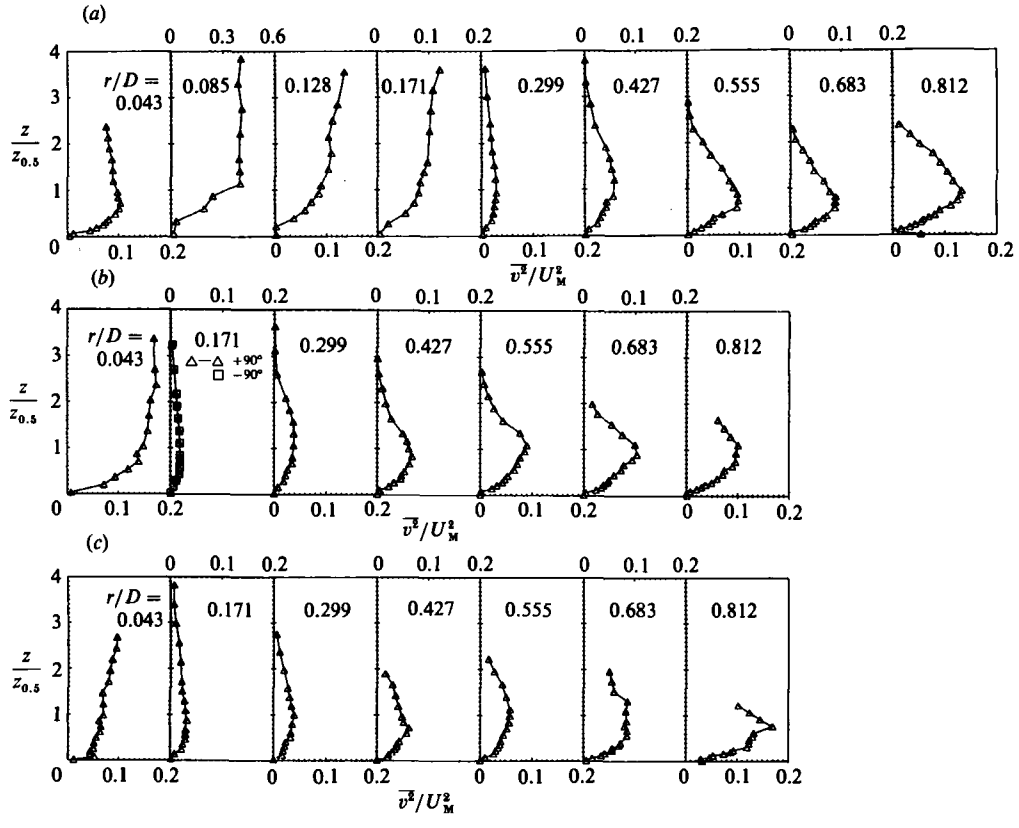

FIGURE 13. Development of the vertical fluctuation intensity profiles along (*a*) $\phi = 0$ line, (*b*) $\phi = 90°$ line, (*c*) $\phi = 180°$ line. $Re_E = 1.3 \times 10^4$, $H/d_E = 22$, $\theta = 20°$.

values for high-order even moments. The large deterministic structures found in the present flow advect the rapid fluctuations of high-intensity eddies so that the temporally intermittent and inhomogeneous flow past the measuring probe volume resulted in distorted distribution of single-point measurements. The skewness coefficient of figure 14 was determined at a wall distance of $z = 10$ mm and provides justification for the distortion of the probability distribution function of the radial velocity. Around the geometrical impingement point, $r/D = 0$, the skewness coefficient is close to zero, indicating that the flow in this region was free from the effects of large deterministic structures with nearly Gaussian probability distribution functions. At large radii, the skewness coefficient tends to a maximum value which is negative along the $\phi = 0$ line, signifying an asymmetrical p.d.f. whose tail extends towards negative values and is positive along the $\phi = 180°$ line. Even though it reduces rapidly along the $\phi = 180°$ line, it tends to remain high along the $\phi = 0$ line suggesting more permanent distortion, as would be expected from figure 3(*b*). The flatness factor shown on the same figure reveals a distribution with positive kurtosis (leptokurtic) far exceeding its normal value of three. It is interesting to note that the flatness factor is relatively larger along the $\phi = 0$ line.

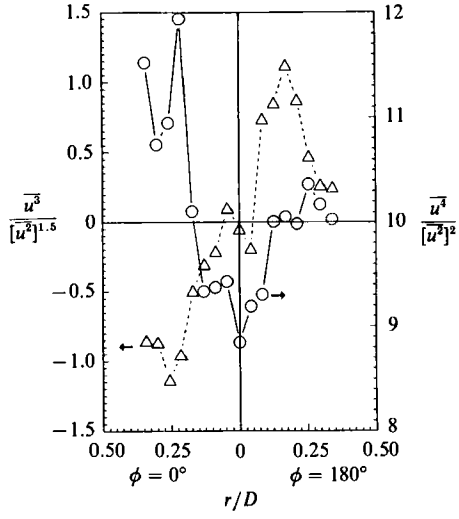

FIGURE 14. Variation of the higher-order moments along the line of incidence at $z = 10$ mm.

3.5. *Temperature field*

To understand the correlation between the mean velocity field and wall heat transfer, the wall temperature distribution was investigated over a symmetrical half-plane ($0 \leqslant \phi \leqslant 180°$) at one side of the line of incidence using liquid-crystal sheets of dimension 200 × 400 mm. The resolution of the commercially available liquid-crystal sheets was relatively poor (~ 3 °C) in the range of wall temperature where cold-wire measurements of impinging air flow were performed (63–101 °C), so that the liquid-crystal experiments involved wall temperatures in a range (33–39 °C) where resolution of around 1 °C was achieved. Figure 15 shows photographs of the wall temperature distribution contours for impingement angles of 0, 10°, 20°, 30°, and 40°, all other conditions being the same. The egg-shaped contour lines are very compact along the $\phi = 0$ line in the close vicinity of the geometrical impingement point and broaden as they are traced azimuthally from $\phi = 0$ to 180°, indicating mild radial temperature gradients for larger values of ϕ. With increase of impingement angle, the symmetry of the normal impingement is distorted and the contour lines are elongated in the $\phi = 180°$. No matter how much they are elongated, the contour lines still give the impression of closed contours surrounding the impingement region, except for $\theta = 40°$ where it is easy to recognize a change in the contour shapes, similar to those of the surface pressure contours of figure 4.

It has been asserted (Sparrow & Minkowycz 1962; Chen, Sparrow & Mucuoglu 1977; Townsend 1972; and Kays & Crawford 1980, pp. 288–331) that the buoyancy forces arising from large temperature differences between the heated horizontal surface and the ambient can induce streamwise pressure gradients and modify the flow. However, the buoyancy parameter, shown in figure 16,

$$\xi = \frac{Gr_r}{Re_r^2}, \quad \text{with} \quad Gr_r = \frac{g\beta(T_w - T_A)r^3}{\nu^2} \quad \text{and} \quad Re_r = \frac{U_M r}{\nu}, \tag{7}$$

(where β is the volumetric coefficient of thermal expansion for air and g is the gravitational acceleration), was negligible over most of the region of interest with values of 0.5 and above confined to very large radial distance, which justifies the assumption that forced convective heat transfer due to the impinging jet dominated

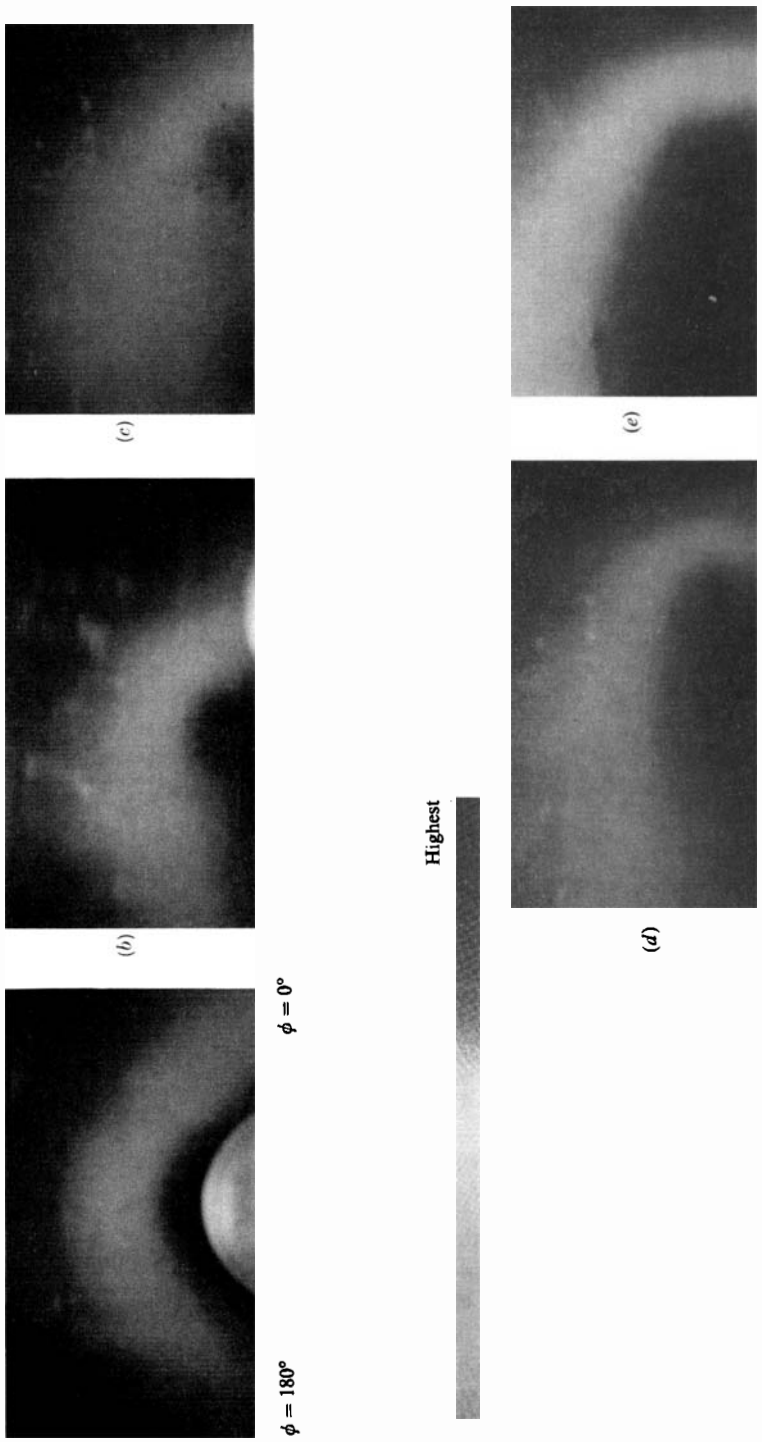

FIGURE 15. Visualization of the surface temperature contours from liquid-crystal colours. (*a*) $\theta = 0$, (*b*) $\theta = 10°$, (*c*) $\theta = 20°$, (*d*) $\theta = 30°$, (*e*) $\theta = 40°$.

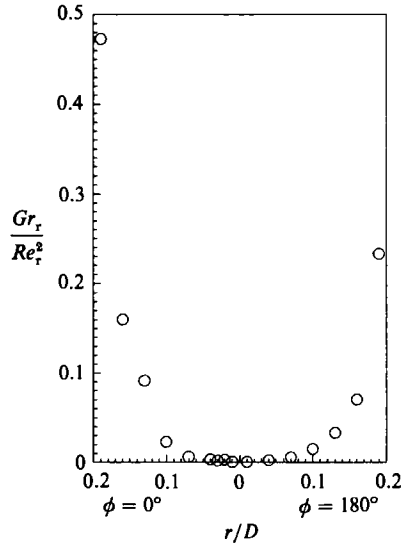

FIGURE 16. Variation of the buoyancy parameter along the line of incidence.

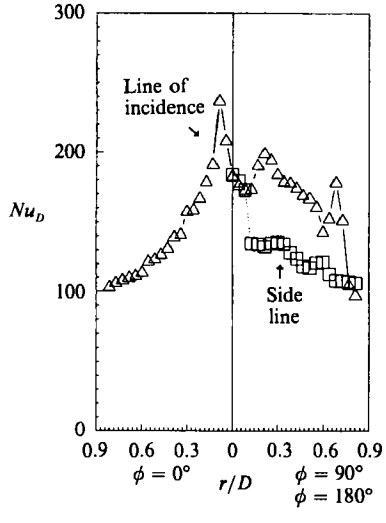

FIGURE 17. Variation of the Nusselt number.

the flow so that cold wire temperature measurements were unaffected. The wall temperature distribution used to calculate the buoyancy parameter and the Nusselt number, $Nu_D = hD/k_a$ (where k_a is the thermal conductivity of air), was extrapolated from the air temperature measured at a wall distance of $z = 0.1$ mm along the line of incidence ($\phi = 0$ and 180° lines) and the side direction ($\phi = 90°$) extending radially to $r/D = 0.812$, assuming that an inner conductive layer exists across which conduction dominates for some distance above the heated wall until convective heat transfer is established. The overall convective heat transfer coefficient, h, was calculated by

$$h = \frac{\dot{Q}''_w}{T_w - T_A} \tag{8}$$

based on the temperature difference between the heated surface and the ambient, and results are shown in figure 17 which reveals that, along the line of incidence, there are two asymmetric maxima on either side of the geometrical impingement point with that in the $\phi = 0$ direction closer to the impingement point. Since the wall heat flux was constant everywhere, these two maxima indicate local increases in the convective heat transfer coefficient due to relatively high velocities involved at the edge of the stagnation bubble, which seems to be distorted towards the $\phi = 180°$ direction, consistent with figure 2. Downstream of these maxima, the Nusselt number decreased with the rise in the surface temperature and, consistent with the liquid-crystal visualization, the radial temperature gradient in the $\phi = 0$ direction was steeper than that in the $\phi = 180°$ direction up to $r/D = 0.55$.

In a similar investigation of unsteady heat transfer resulting from normal impingement of a jet onto a heated plate initially at a uniform temperature, Donaldson *et al.* (1971) showed that convective heat transfer depended on radial distance so that, at large Reynolds numbers, the stagnation point heat transfer was small compared to the wall jet heat transfer in the immediate vicinity of the geometrical impingement point, resulting in an initial rise in heat transfer with radial distance before the decrease further downstream. Since the thermal boundary condition in the impingement plane was different in their experiments, it is difficult to relate the two sets of results except that the trend of their convective heat transfer with radial distribution resembles that of the present experiments. The present results also show that the rate of the decrease of h at large radial distances is very different on either side of the geometrical impingement point. A third maximum occurred along the $\phi = 180°$ line at $r/D = 0.683$, following which the Nusselt number rapidly reached the level found along the $\phi = 0$ line at the same radial position. The maximum at $r/D = 0.683$ again confirmed the presence of the large stationary structure revealed in the flow visualization and the vertical velocity profiles. It was concluded that the strong vortical motion induced by this structure brought the outer relatively colder fluid to the wall and raised hot fluid away from the wall, causing local augmentation of the convective heat transfer coefficient. Results in the $\phi = 90°$ and 180° directions were similar but with smaller magnitudes in the latter.

The temperature profiles along the line of incidence, figure 18, show the development of a very weak peak away from the wall, consistent with temperature stratification in which a stream of a relatively colder fluid is sandwiched between two hot streams with the lower at the higher temperature. At large radial distances, along the $\phi = 0$ and 180° directions, the second peak becomes stronger and extends into the free shear layer and towards the wall to cause local flattening of the temperature profile between $z/z_p = 2.5$ and 6 with disappearance of the colder stream. Further downstream, this plateau disappears resulting in a profile of smoothly decreasing temperature. It can be conjectured that the thin cold layer is associated with the presence of a temperature gradient in the large structures as they are convected downstream. As the outer region of the vortices contacts the wall just downstream of the impingement point, where the Nusselt number is also a maximum, it picks up thermal energy and forms a layer surrounding the fluid deflected from the core of the inflowing jet without interaction with the wall. As the vortices pass by, the colder region encapsulated within the peripheral hot layer biasses the time-averaged readings of a fixed probe towards lower temperatures, and this effect increases with z up to the vortex centre and then decays. The temperature of fluid near the vortex centre remains unaffected for a short distance as the vortices are advected along the wall jet, since the large-scale convective motion near the vortex centre is unable to

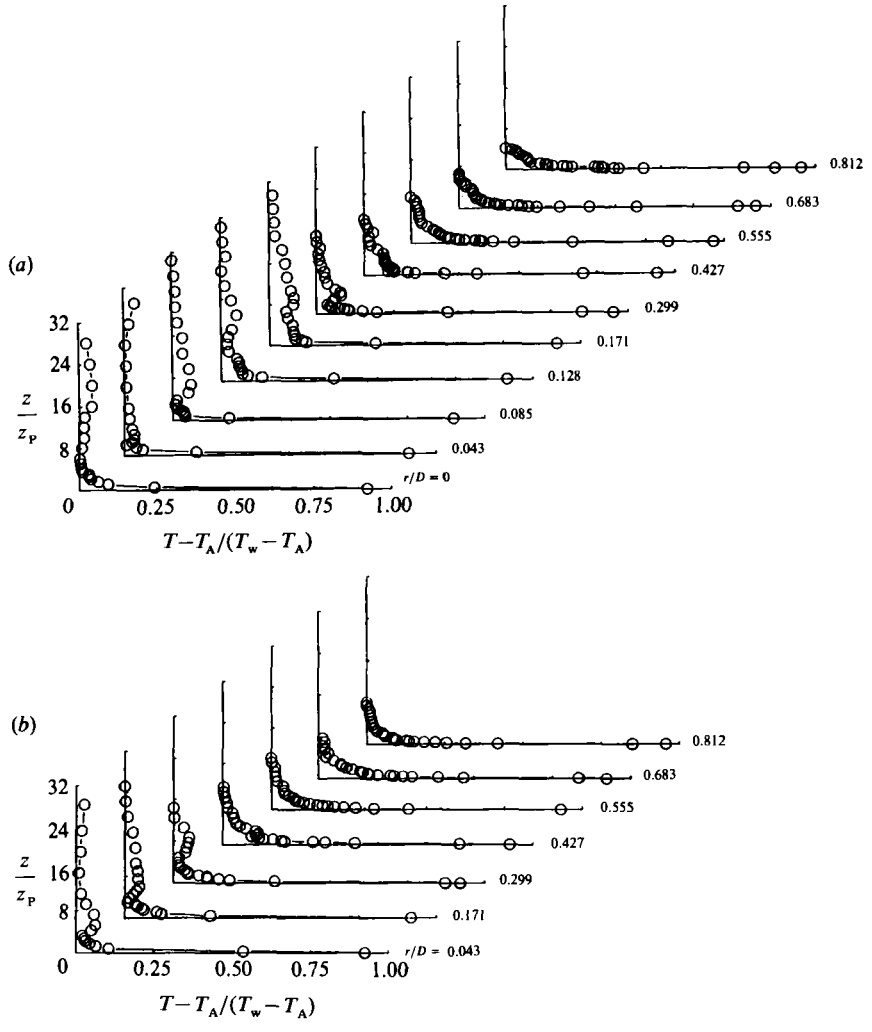

FIGURE 18. Development of the temperature profiles along the line of incidence; (*a*) $\phi = 0$ line including $r = 0$ (*b*) $\phi = 180°$ line. $Re_E = 1.3 \times 10^4$, $H/d_E = 22$, $\theta = 20°$.

enhance the lateral transport of a passive scalar. The diffusive penetration, however, gradually eliminates the isolated local cold layer further downstream and this shows that, when the convection of the large coherent structures follows a regular path, it can cause an inactive zone where the transport of the passive scalars is due only to gradient-type diffusion.

It is well known, for example Townsend (1976), that the absence of advection in the balance of thermal fluctuation intensity can imply a thermal equilibrium layer in which the local gradient of the mean temperature depends only on distance from the wall and on the distribution of the heat flux, $\dot{q}''$, and the total shear stress, τ_t. Provided that the ratio, $\dot{q}''/\tau_t^{\frac{1}{2}}$, remains constant (see also the Appendix), the temperature distribution in the thermal equilibrium layer can be expressed by the law of the wall in terms of wall shear stress τ_w, and wall heat flux $\dot{q}''_w$, as

$$\frac{\kappa_T \tau_w^{\frac{1}{2}}(T_w - T)}{\dot{q}''_w} = \ln\left(\frac{\kappa_T \tau_w^{\frac{1}{2}} z}{\nu}\right) + A. \tag{9}$$

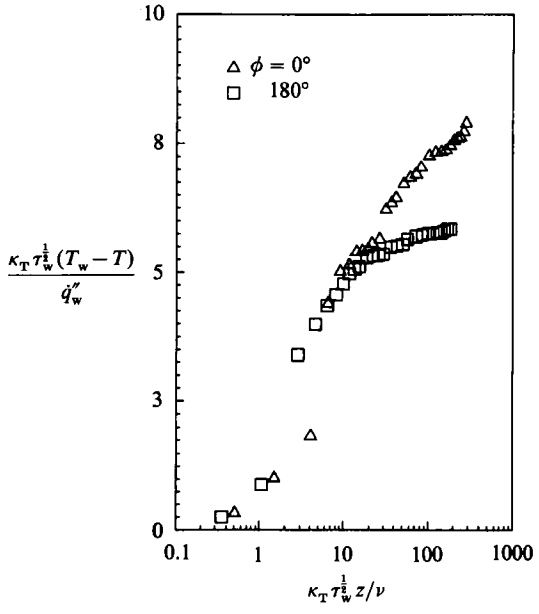

FIGURE 19. Semilogarithmic plot of the temperature profiles at $r/D = 0.812$.

The existence of a thermal equilibrium layer was considered in relation to temperature profiles at $r/D = 0.812$ and $\phi = 0$ and 180° where the profiles are nearly fully developed. Figure 19 shows a large region of conductive layer next to the wall, confirming that the first measurement point lies well within the conductive layer with an equilibrium layer represented by a logarithmic temperature variation with distance from the wall. It is apparent that the conductive and equilibrium layers are larger at the $\phi = 0$ side and that the equilibrium layer extends to the free shear layer far from the wall. The functional form of the law of the wall, however, seems to be invariant at two positions along the $\phi = 0$ and 180° lines.

The general characteristic of the profiles of the temperature fluctuation intensity, $(T_{rms}/T_w)^2$, figure 20, is a peak close to the wall followed by a smooth decrease to a constant level at large wall distances. The plateau corresponds to the temperature fluctuations at ambient conditions and increases with radius from 7 mV, corresponding to the r.m.s.-noise level of the cold-wire system, to a value of 12 mV. Since the noise level of the cold-wire system is constant, the results indicate a progressive broadening in the temperature p.d.f. of the ambient fluid just above the wall jet with the radial distance, and this implies a mixing mechanism of the second type (Perry *et al.* 1980) in which the ambient fluid is first infected by the intermittent thermal fluctuations before the mean temperature is acquired. Considering this level as the boundary of the domain in which the effect of heating is important for a thermodynamic processes such as evaporation, it can be seen that the absolute magnitude of the temperature fluctuations increases at large radial distances, while the thermal penetration from the plate advances in a direction normal to the wall. The evolution of the fluctuation profiles confirms the conjecture that the virtual origin of the thermal activity is behind the geometrical impingement point.

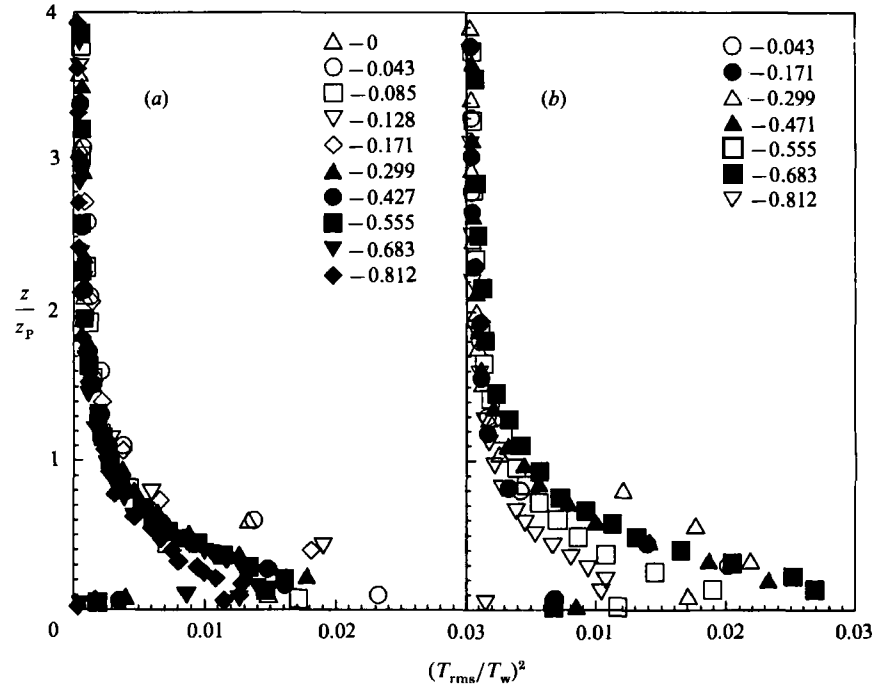

FIGURE 20. Development of the temperature fluctuation intensity profiles along the line of incidence at the r/D values indicated: (*a*) $\phi = 0$ line including $r = 0$, (*b*) $\phi = 180°$ line. $Re_E = 1.3 \times 10^4$, $H/d_E = 22$, $\theta = 20°$.

4. Conclusions

4.1. *Aerodynamic aspects*

The radial wall flow field formed after angled impingement of a round turbulent jet was found to depend on the angle of impingement, with a sudden change of the orientation of the surface pressure contours at $\phi = 40°$. Mean-flow characteristics of the radial wall flow such as velocity decay and growth rate, exhibit strong azimuthal dependence for all values of θ, as has been shown in terms of contours of surface pressure and streaks of pigmented oil. Oblique impingement also introduces vertical velocities so that boundary-layer approximations are inapplicable, even for values of θ less than 40°.

The radial velocity profiles asymptote to an analytical function which has slight dependence on the azimuthal coordinate, ϕ, and this is achieved most rapidly in the direction of the inflowing jet ($\phi = 180°$). The long-lasting effect of the inflexion point in the inner layer, most in evidence along the $\phi = 0$ and 90° directions, contributes to the inviscid flow instability (mean-profile-dependent instability) to generate spatially coherent structures which were most pronounced at an impingement angle of 20°. It has been conjectured that these structures are a consequence of a collective interaction of two or more ring vortices of the inflowing free jet, asymmetrically distorted due to the exposure of the asymmetric strain field in the impingement region. These structures are important to the large-scale convective transport of passive scalars such as concentration and temperature and enhance mixing by engulfing quiescent fluid, since the gradient-type diffusive transport by small-scale turbulence and molecular actions is weak particularly in the vicinity of the

impingement point. However, the fluid in the inactive zone near the vortex centre acquires the passive marker only by the latter transport mechanism.

At large radii, the radial mean velocity profiles have a logarithmic region extending up to the point of the velocity maximum provided that the local flow development is represented by a deviation function, $A(U_M/U_\tau)$, similar to that for flow over rough surfaces with adverse pressure gradient. The deviation function has a weak dependency on the azimuthal coordinate, ϕ.

4.2. *Thermal aspects*

With angled impingement, the Nusselt number has an azimuthal dependence in accordance with the variation of surface temperature, which exhibits a sudden change at $\phi = 40°$ in parallel with the dynamics of the flow in the close vicinity of the wall.

The thermal gradient inside the vortices advected downstream has been shown to bias the measured time-averaged temperature towards lower values which are perceived in the mean profiles as temperature stratification with a relatively colder stream between two hot streams. If the temperature information is envisaged as mass concentration, as in the engine application, this layer corresponds to low values which would lead to locally inhomogeneous mixtures of fuel just downstream of the impingement point. With the disappearance of stratification, a conductive and a thermal equilibrium layer become apparent in the mean temperature profile. In contrast to the momentum equilibrium layer, the thermal equilibrium layer has a functional form which is invariant at two positions along the $\phi = 0$ and 180° lines where the effect of the stagnation region is eliminated. It is noteworthy that the conductive and thermal equilibrium layers are larger than the corresponding viscous and momentum equilibrium layers and, in particular, the thermal equilibrium layer extends deep into outer free shear layer so that the outer edge of the thermal equilibrium layer along the $\phi = 0$ side, for example, occurs at $z = 16.3$ mm while the velocity maximum occurs at $z = 6.4$ mm.

Considering the mechanisms of the generation and the subsequent lateral flux of momentum and thermal energy, it appears that the difference in the behaviour of the aerodynamic and thermal equilibrium layers of the wall jet flow stems from the conditions imposed at the lower and upper boundaries. The wall jet had heat input only from the wall so that the lateral flux of thermal energy was down the mean gradient towards the quiescent ambient. However, the velocity field had two sources of momentum generation at the wall and at the interface with the quiescent ambient and, thus, the resulting penetration from both sources was inwards to the domain so that the lateral flux of momentum was no longer negligible relative to the production and dissipation. Townsend (1976) shows that this situation can result in a momentum equilibrium layer with variable stress which lies over a very large region and that this is realized by flows with adverse pressure gradient. These are the symptoms exactly fulfilled in the radially decelerating wall jet.

This research was supported through grants from Ford Motor Co., UK Ltd. The authors would like to thank Dr C. Arcoumanis for his assistance in various stages of this investigation.

Appendix

If the influence of advective processes is negligible on the balance of thermal fluctuation intensity, the thermal structure depends only on three parameters: the local heat flux $\dot{q}''$, distance from the wall z, and the local total shear stress τ_t, i.e.

$$\frac{\partial T}{\partial z} = g(\dot{q}'', z, \tau_t), \tag{A 1}$$

where g represents an arbitrary functional relationship. Following the method of Rayleigh (Olivari 1988), it can be supposed that

$$\frac{\partial T}{\partial z} = \alpha_1((\dot{q}'')^{\alpha_2}(z)^{\alpha_3}(\tau_t)^{\alpha_4}), \tag{A 2}$$

where $\alpha_1, \alpha_2. \alpha_3$, and α_4 are pure numbers, and the dimensions of the variables depend on the fundamental dimensions of the problem, i.e. length L, time t, and temperature F. If (A 2) is to be physically consistent, it must be dimensionally homogeneous which implies that the exponents of length, time, and temperature on both sides of (A 2) should be equal, leading to the values, $\alpha_2 = 1$, $\alpha_3 = -1$, and $\alpha_4 = -\frac{1}{2}$ and, hence, to

$$\frac{\partial T}{\partial z} = -\frac{1}{\kappa_T}\frac{\dot{q}''}{(\tau_t)^{\frac{1}{2}}z}, \tag{A 3}$$

where α_1 is set equal to $-1/\kappa_T$, with κ_T the Kármán constant for thermal diffusion.

If the ratio, $\dot{q}''/\tau_t^{\frac{1}{2}}$, is constant, (A 3) integrates to the logarithmic distribution of mean temperature which can be put in the form

$$\frac{\kappa_T \tau_t^{\frac{1}{2}}(T_w - T)}{\dot{q}''} = \ln\left\{\frac{\kappa_T \tau_t^{\frac{1}{2}} z}{\nu}\right\} + \Delta, \tag{A 4a}$$

where Δ represents the temperature jump across the conductive layer and is given as

$$\Delta = \ln\left\{\frac{\nu}{\kappa_T \tau_w^{\frac{1}{2}} z_c}\right\} + \frac{\kappa_T \tau_w^{\frac{1}{2}}(T_w - T|_{z=z_c})}{\dot{q}_w''}. \tag{A 4b}$$

The analysis shows that, since the ratio, $\dot{q}''/\tau_t^{\frac{1}{2}}$, remains constant, for the heat flux between the layers parallel to the wall to be constant, i.e. $\dot{q}'' = \dot{q}_w''$, there should be a region of constant shear stress, $\tau_t = \tau_w$, which, in turn, implies the presence of a momentum equilibrium layer as large as the thermal equilibrium layer. As shown in §3.4, this is not the case. However, provided that the conductive layer extends beyond the viscous sublayer, the conditions at the edge of the viscous sublayer, $\tau_t = \tau_w$ and $\dot{q}'' = \dot{q}_w''$, which also specify the boundary conditions at the wall, fully describe the aspects of the motion relevant to the transport of heat and are realized as

$$\frac{\dot{q}''}{\tau_t^{\frac{1}{2}}} = \left.\frac{\dot{q}''}{\tau_t^{\frac{1}{2}}}\right|_{z=z_v} = \frac{\dot{q}_w''}{\tau_w^{\frac{1}{2}}}. \tag{A 5}$$

thus, (A 4a, b) can be written in the final form

$$\frac{\kappa_T \tau_w^{\frac{1}{2}}(T_w - T)}{\dot{q}_w''} = \ln\left\{\frac{\kappa_T \tau_w^{\frac{1}{2}} z}{\nu}\right\} + \Delta, \tag{A 6a}$$

and

$$\Delta = \ln\left\{\frac{\nu}{\kappa_T \tau_w^{\frac{1}{2}} z_c}\right\} + \frac{\kappa_T \tau_w^{\frac{1}{2}}(T_w - T|_{z=z_c})}{\dot{q}_w''}. \tag{A 6b}$$

REFERENCES

ABRAMOVICH, G. N. 1963 *The Theory of Turbulent Jets.* MIT Press.

BAKKE, P. 1957 An experimental investigation of a wall jet. *J. Fluid Mech.* **2**, 467–472.

BRADSHAW, P. & LOVE, E. M. 1959 The normal impingement of a circular air jet on a flat plate. *Aero. Res. Counc. Rep.* 21, p. 268.

CHEN, T. S., SPARROW, E. M. & MUCUOGLU, A. 1977 Mixed monvection in boundary layer flow on a flat plate. *Intl J. Heat Transfer* **99**, 66–71.

CLAUS, R. W. & VANKA, S. P. 1990 Multigrid calculations of a jet in crossflow. *AIAA*-90-0444.

DIDDEN, N. & HO, C. M. 1985 Unsteady separation in an impinging jet. *J. Fluid Mech.* **160**, 235–256.

DONALDSON, C. DUP. & SNEDEKAR, R. S. 1971 A study of free jet impingement. Part 1. Mean properties of free and impinging jets. *J. Fluid Mech.* **45**, 281–319.

DONALDSON, C. DUP., SNEDEKAR, R. S. & MARGOLIS, D. P. 1971 A study of free jet impingement. Part 2. Free jet turbulent structure and impingement heat transfer. *J. Fluid Mech.* **45**, 477–512.

FOSS, J. F. 1979 Measurements in a large-angle oblique jet impingement flow. *AIAA J.* **17**, 801–802.

FOSS, J. F. & KLEIS, S. J. 1976 Mean flow characteristics for the oblique impingement of an axisymmetric jet. *AIAA J.* **14**, 705–706.

FOUNTI, M. & LAKER, J. 1981 Performance characteristics of a new frequency counter interfaced to a micro-processor controlled data acquisition and processing system. *Imperial College Mech. Engng Rep.* FS/81/36.

GLAUERT, M. B. 1956 The wall jet. *J. Fluid Mech.* **1**, 625–643.

GUTMARK, E., WOLFSHTEIN, M. & WYGNANSKI, I. 1978 The plane turbulent impinging jet. *J. Fluid Mech.* **88**, 737–756.

HEAD, M. R. & BANDYOPADHYAY, P. 1981 New aspects of turbulent boundary-layer structure. *J. Fluid Mech.* **107**, 297–338.

HINZE, J. O. 1959 *Turbulence, An Introduction to its Mechanism and Theory.* McGraw-Hill.

HO, C. M. & NOSSEIR, N. S. 1980 Large coherent structures in an impinging jet. In *Turbulent Shear Flows 2* (ed. J. S. L. Bradbury, F. Durst, B. E. Launder, F. W. Schmidt & J. H. Whitelaw), pp. 297–304, Springer.

HO, C. M. & NOSSEIR, N. S. 1981 Dynamics of an impinging jet. Part 1. The feedback phenomenon. *J. Fluid Mech.* **105**, 119–142.

HUSAIN, Z. D. & HUSSAIN, A. K. M. F. 1979 Axisymmetric mixing layer: Influence of the initial and boundary conditions. *AIAA J.* **17**, 48–55.

IRWIN, H. P. A. 1973 Measurements in a self-preserving plane wall jet in a positive pressure gradient. *J. Fluid Mech.* **61**, 33–63.

KAYS, W. M. & CRAWFORD, M. E. 1980 *Convective Heat and Mass Transfer*, 2nd edn. McGraw-Hill.

KESTIN, J. & WOOD, R. T. 1969 Enhancement of stagnation-line heat transfer by turbulence, *Progr. in Heat and Mass Trans.* **2** 249, Pergamon-Oxford.

KREID, D. K. 1974 Laser-doppler velocimeter measurements in nonuniform flow: Error estimates. *Appl. Opt.* **13** 1872–1881.

LANDRETH, C. C. & ADRIAN, R. J. 1990 Impingement of a low Reynolds number turbulent circular jet onto a flat plate at normal incidence. *Exp. Fluids* **9**, 74–84.

MELE, P., MORGANTI, M., SCIBILIA, M. F. & LASEK, A. 1986 Behavior of wall jet in laminar-to-turbulent transition. *AIAA J.* **24**, 938–939.

OLIVARI, D. 1988 *Theory of Models, Course Notes on Applied Fluid Mechanics.* von Karman Institute For Fluid Dynamics, Rhode-St-Genese, Belgium.

OTTINO, J. M. 1989 *The Kinematics of Mixing: Stretching, Chaos, and Transport.* Cambridge University Press.

ÖZDEMİR, İ. B. 1992 Impingement of single- and two-phase jets on unheated and heated flat plates. Ph.D. Thesis, University of London.

PERRY, A. E., LIM, T. T. & CHONG, M. S. 1980 The instantaneous velocity fields of coherent structures in coflowing jets and wakes. *J. Fluid Mech.* **101**, 243–256.

PERRY, A. E., SCHOFIELD, W. H. & JOUBERT, P. N. 1969 Rough wall turbulent boundary layers. *J. Fluid Mech.* **37**, 383–413.

POREH, M., TSUEI, Y. G. & CERMAK, J. E. 1967 Investigation of a turbulent radial wall jet. *Trans. ASME* E: *J. Appl. Mech.* **34**, 457–463.

SCHMIDT, G. & TONDL, A. 1986 *Non-linear Vibrations.* Cambridge University Press.

SCHWARZ, W. H. & COSART, W. P. 1961 The two-dimensional turbulent wall jet. *J. Fluid Mech.* **10**, 481–495.

SPARROW, E. M. & MINKOWYCZ, W. J. 1962 Buoyancy effects on horizontal boundary-layer flow and heat transfer. *Intl J. Heat Mass Transfer* **5**, 505–511.

TAILLAND, A. & MATHIEU, J. 1967 Jet parietal. *J. Méc.* **6**, 105–131.

TAYLOR, G. I. 1960 Formation of thin flat sheets of water. *Phil. Trans. R. Soc. Lond.* A **259**, 1–17.

TAYLOR, G. I. 1966 Oblique impact of a jet on a plane surface. *Phil. Trans. R. Soc. Lond.* A **260**, 96–100.

TOWNSEND, A. A. 1972 Mixed convection over a heated horizontal plate. *J. Fluid Mech.* **55**, 209–227.

TOWNSEND, A. A. 1976 *The Structure of Turbulent Shear Flows*, 2nd Edn. Cambridge University Press.

TSUJI, Y., MORIKAWA, Y. & SAKOU, M. 1977*a* The stability of a radial wall jet. *Aeronaut. Q.* **28**, 247–258.

TSUJI, Y., MORIKAWA, Y., NAGATANI, T. & SAKOU, M. 1977*b* The stability of a two-dimensional wall jet. *Aeronaut. Q.* **28**, 235–246.

WESTLEY, R., WOOLLEY, J. H. & BROSSEAU, P. 1972 Surface pressure fluctuations from jet impingement on an inclined flat plate. *AGARD Symp. Acoustic Fatigue, AGARD-CP-113.*

ZAMAN, K. B. M. Q. & HUSSAIN, A. K. M. F. 1980 The mechanics of vortex pairing in an axisymmetric mixing layer. In *Turbulent Shear Flows 2* (ed. J. S. L. Bradbury, F. Durst, B. E. Launder, F. W. Schmidt & J. H. Whitelaw), pp. 327–343. Springer.